ACS APPLIED ENERGY MATERIALS

www.acsaem.org Article

Electronic Structure, Chemical Bonding, and Electrocatalytic Activity of $Ba(Fe_{0.7}Ta_{0.3})O_{3-\delta}$ Compounds

C. V. Ramana,* Mallesham Bandi, Aruna N Nair, Felicia S. Manciu, Sreeprasad Sreenivasan, and Vaithiyalingam Shutthanandan

Cite This: *ACS Appl. Energy Mater.* 2021, 4, 1313−1322 Read Online

ACCESS | Metrics & More | Article Recommendations

ABSTRACT: $Ba(Fe_{0.7}Ta_{0.3})O_{3-\delta}$ (BFTO) compounds were synthesized using a conventional, high-temperature solid-state ceramic reaction method by varying the sintering temperature (T_s = 1200−1350 °C). The crystal structure, electronic structure, and electrocatalytic activity of BFTO compounds were evaluated. The processing temperature induced phase transformations and structural quality influences the electronic structure and electrocatalytic activity of BFTO compounds. At T_s = 1200 °C, $Ba(Fe_{0.7}Ta_{0.3})O_{3-\delta}$ stabilizes as a mixture of the orthorhombic + rhombohedral phase ($Amm2$ + $R3m$). With increasing T_s (≥1250 °C), $Ba(Fe_{0.7}Ta_{0.3})O_{3-\delta}$ ceramics stabilize in tetragonal + rhombohedral [$P4mm$ + $R3m$] mixed phase with a variation in the number of respective phases. High-resolution X-ray photoelectron spectroscopy (XPS) of constituent elements, namely, Ba 3d, Fe 2p, Ta 4f, and O 1s levels reveals the electronic structure changes due to changes in the chemical environment resulted from structural transformation. The XPS analyses indicate that the processing temperature significantly influences the chemical environment of Fe and Ta cations in BFTO. The Ba $3d_{5/2}$ core-level XPS spectra indicate that the perovskite phase gradually increases with increasing sintering temperature. The presence of absorption bands that are exclusively due to MO_6 stretching vibration that is connected to Ba ion as well as stretching of M−O bonds in infrared spectroscopy data indicate the structural and chemical quality of the BFTO compounds. The electrocatalytic activity of BFTO was evaluated toward hydrogen evolution reaction (HER) and oxygen reduction reaction (ORR). Though all of the samples demonstrated appreciable electrocatalytic properties, the best electrochemical catalytic activity was shown by BFTO samples sintered at 1350 °C. BFTO-1350 °C showed an onset potential of −0.690 V vs reversible hydrogen electrode (RHE) for HER and an onset potential of 0.73 V vs RHE for ORR indicating its significant electrocatalytic performance. A general increase in activity with sintering temperature is potentially due to the improved structural quality of the BFTO ceramics. In addition to offering the fundamental insights into perovskite materials based on co-doped $BaTiO_3$ for electrocatalysis, the present work may contribute to the design and development of materials using co-doping of different chemical valence cations for other energy-related applications.

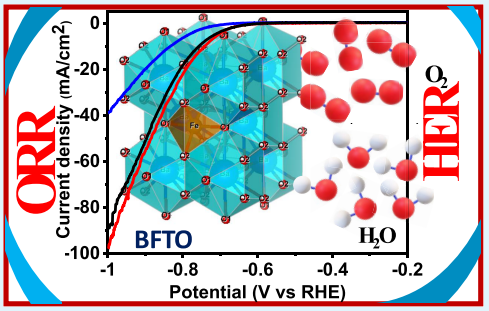

KEYWORDS: *$Ba(Fe_{0.7}Ta_{0.3})O_{3-\delta}$, phase transformation, electronic structure, XPS, electrocatalytic activity, hydrogen evolution reaction, oxygen reduction reaction*

1. INTRODUCTION

Perovskite oxides, which constitute wide range of compositions, are earth-abundant and offer excellent means to realize chemical compounds, especially in the field of catalysis, that are economically viable and versatile in terms of technological or industrial applications.[1−9] The perovskite oxides find interesting applications in current and emerging electronics and electro-optics,[10−13] electrochemical science and technology,[10,11,14−17] electromechanical sensors and systems,[11,12] solid oxide fuel cell technology,[5,14,18] electromagnetic devices and magnetic tunnel junctions,[10−13,19] and solid-state memory device technologies.[10−13,19−21] The perovskite oxide-based piezoelectric materials are attractive for a number of applications in micromechanics, sensors, actuators, optoelectronics, and energy-harvesting applications.[1,3,19,20] Especially, the piezoelectric and ferroelectric properties, which often exist in the same perovskite oxide matrix, provide excellent means to harvest energy from multiple sources, which include mechanical, electrical, chemical, vibration, and optical.[20] The dominance of oxide perovskites in the electromechanical and sensor technological applications and development is mostly due to their superior properties, such as high Curie temperature (T_c ≈ 390 °C), high dielectric constant (ε ∼

Received: October 16, 2020
Accepted: December 23, 2020
Published: January 19, 2021

20 000 at T_c), low dielectric loss ($\tan\delta \sim 0.004$), and high piezoelectric coefficient ($d_{33} \sim 220$ pC/N).[21−23]

The crystal structure of a perovskite (ABO_3; Figure 1) is named after the mineral perovskite $CaTiO_3$. The structure of

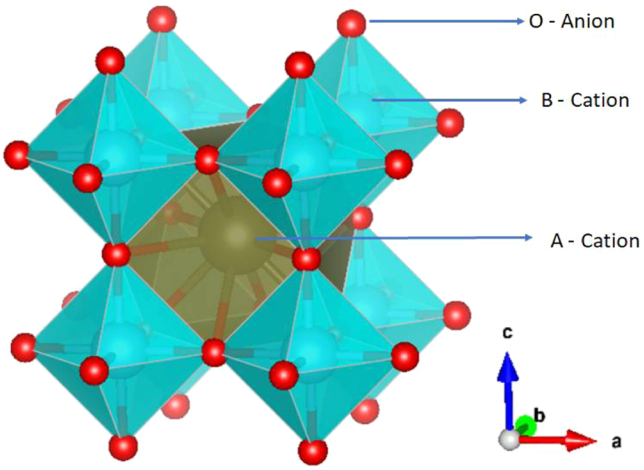

Figure 1. Ideal crystal structure of perovskite oxide with a general chemical formula of ABO_3. The A-, B-, and O-ions are indicated in the figure.

an ideal perovskite consists of a cubic unit cell with an A-site species located at [1/2,1/2,1/2], B-site species at [0,0,0], and oxygen located at [1/2,0,0] resulting in the B-site species forming a sublattice of six-coordinate, vertex-sharing octahedra and A-site species forming a sublattice of 12-coordinate face-sharing cuboctahedra[24,25] (Figure 1). However, the ideal perovskite cubic structure may be distorted depending on the size of the A and B cations.[16,24] From a structure point of view, the most notable feature is their versatility of accommodation. This primarily stems from flexible or adoptable structures that can be easily manipulated by means of doping various elements at the A- and B-sites of the perovskite structure (ABO_3).[16,24]

The objective of the present work is to elucidate the electronic structure, chemical valance states of various cations, chemical bonding, and electrocatalytic activity of Fe, Ta co-doped perovskite structured oxides, namely $Ba(Fe_{1-x}Ta_x)O_{3-\delta}$ compounds. The origin of these materials is primarily due to the design and development of high-temperature operating, yet temperature independent, chemical sensors.[26−29] Due to high melting point and decomposition temperature, perovskite oxides based on Sr and Ba have been studied both in the form of bulk and thin films[26−29] for high-temperature sensors in catalytic converters, electrode materials in fuel cells, and photocatalysts in energy conversion technologies. In fact, the high melting point and decomposition temperatures of these materials generally provide unparalleled microstructural stability, which is an important requirement for considering them for practical applications in photo- and electrocatalysis, in addition to high-temperature chemical sensors. Moreover, the specific ability of doping of different cations at the A- and B-sites allows the design and development of materials with wide range of compositions that can facilitate tuning the electronic structure and properties desirable for applications in the field of catalysis.[10−13,30,31] For instance, Cr/Nb- and Cr/Ta-doped $SrTiO_3$ showed higher activities and shorter induction periods than just Cr-doped $SrTiO_3$.[32−35] Based on the chemical bonding and electronic structure analyses, it was demonstrated that the formation of Cr^{6+} ions, which act as charge recombination centers, was fully suppressed by co-doping of Ta ions.[36] Cr/Ta-doped $SrTiO_3$ still showed higher activity than Cr-doped $SrTiO_3$ even when H_2 reduction was conducted to reduce Cr^{6+}. It is due to that the formation of oxygen defects was also suppressed by co-doping of Ta ions since the charge balance in the crystals was maintained by substitution of a couple of Cr^{3+}/Ta^{5+} for two Ti^{4+} ions. Thus, it has been found that Nb and Ta ions are efficient co-dopants[32−34] to maintain the charge balance when titanate-based catalysts are modified by doping of the low valence ions such as Cr^{3+}. Based on these considerations, Ta was chosen to work with co-doping of Fe, while the primary reasons for Fe-based perovskites are derived from the following considerations.

The electrocatalytic activity of Fe-based perovskites has been explored for water electrolysis involving the oxygen evolution reaction (OER) as documented widely in the literature.[37−39] The Sr-doped La-based perovskite oxide catalysts ($La_{1-x}Sr_xFeO_{3-\delta}$) have been studied by She et al.[37] The enhanced OER-specific activity of these doped compounds compared to the parent compound ($LaFeO_{3-\delta}$) was attributed to the optimized surface oxygen vacancies and surface Fe oxidation states.[37] Also, a remarkable enhancement in OER activity has been reported in Si-doped $SrFeO_{3-\delta}$.[38] The enhancement in OER activity originated from the structural transition-driven optimized Fe oxidation state, rich oxygen vacancies, and fast charge transfer.[38] Kim et al., studied the Fe-doped Co-based perovskites; these compounds exhibit extraordinary OER activities and stabilities when Co is partially doped with Fe.[39] The enhanced electrochemical performance is attributed to Fe-induced charge stabilization of Co in a lower oxidation state, maximization of perovskite oxide surface, and stability of perovskite oxide structure.[39] Furthermore, in our recent work, we reported an approach to derive electrocatalytic activity, which is otherwise not possible, in oxide materials.[40] Iron-mixed Ga-oxide demonstrated appreciable electrocatalytic activity toward the generation of H_2 through electrocatalytic water splitting.[40] The electrocatalytic activity of Fe-doped Ga-oxide compounds is attributed to the cumulative effect of different mechanisms, such as Fe-doping induced new catalytic centers and enhanced conductivity due to Fe chemical states.[40] In view of these considerations, the present work was focused toward the synthesis, electronic structure determination, and electrocatalytic activity evaluation of Fe, Ta co-doped BFTO compounds. From electrocatalysis point of view, the scientific merit and significance of the present work can be further understood as follows.

Precious metals like platinum (Pt) are typically used to catalyze sluggish electrochemical reactions that are critical to renewable energy technologies, such as oxygen reduction reaction (ORR) and hydrogen evolution reaction (HER). However, the high price and low abundance of Pt limit its extensive use. Therefore, a viable alternate low-cost electrocatalyst for HER as well as for ORR has attracted increasing interest in renewable energy research. In this direction, perovskite oxides of transition metals are considered as promising alternatives in this regard and hence activating and optimizing non-noble metals for HER is an alternative way for low-cost hydrogen production.[2,4,5,35−42] Non-precious-metal-based electrocatalysts also attracted intense attention as a suitable electrocatalyst toward ORR due to its high activity and better stability.[43−45] Therefore, in the present work, in addition

https://dx.doi.org/10.1021/acsaem.0c02548
ACS Appl. Energy Mater. 2021, 4, 1313−1322

to evaluating the structure and electronic properties of Fe, Ta co-doped oxide, we performed studies to evaluate the electrocatalytic activity toward HER and ORR.

2. EXPERIMENTAL DETAILS

2.1. Synthesis of BFTO Compounds. $Ba(Fe_{0.7}Ta_{0.3})O_{3-\delta}$ [BFTO30] compounds were synthesized using the conventional high-temperature solid-state chemical reaction method. High-purity precursor materials, namely, $BaCO_3$ (99.9%, Sigma-Aldrich), Fe_2O_3 (99.9%, Sigma-Aldrich), and Ta_2O_5 (99.9%, Sigma-Aldrich) were weighed in stoichiometric proportion to achieve a desired composition. Stoichiometrically weighed precursors were homogeneously grounded in an agate mortar using acetone as wetting media. Then, the grounded powders were calcined at different temperatures (1000, 1050, 1100, and 1150 °C) with intermediate grinding to achieve phase purity. The calcination time was 8 h, which was maintained constant for all of the samples. The calcined powders were regrounded to decrease the particle size, and the fine powder was pelletized using a die and uniaxial hydraulic press by applying a load of 1.5 ton in the form of a circular disc (diameter—8 mm and thickness—1 mm). The pellets were sintered in a muffle furnace at different sintering temperatures (T_s) 1200, 1250, 1300, and 1350 °C. The sintering time was set to 8 h, which was again maintained constant for all of the BFTO samples. All of the sintered BFTO samples were further characterized using X-ray diffraction, X-ray photoelectron spectroscopy, Fourier transform infrared spectroscopy, and electrocatalytic studies.

2.2. Characterization. *2.2.1. X-ray Diffraction (XRD).* The X-ray diffraction (XRD) measurements were made using Rigaku X-ray diffractometer [Mini Flex II]. Both calcined and sintered samples were analyzed at room temperature. The XRD parameters employed were: 10−80° (2θ range), step size—0.02°, and scan rate—0.6°/min.

2.2.2. X-ray Photoelectron Spectroscopy (XPS). X-ray photoelectron spectroscopy (XPS) was used to probe the electronic structure and chemical bonding information in BFTO compounds. BFTO samples sintered at various temperatures were analyzed using XPS measurements, which include survey scans as well as high-resolution, detailed core-level scans of respective elements and/or cation in BFTO. A calibrated Kratos Axis Ultra DLD spectrometer (Kratos Analytical, Manchester, U.K.) which has a high-performance Al Kα (1486.7 eV) spherical mirror analyzer is used in this study to analyze the BFTO samples. Prior to taking the samples into the XPS chamber, they were mounted on a Cu stub using a double-sided Cu tape. A charge neutralizer was used to compensate for the remnant surface charging effects. The Cu tape attached to the sample surface connecting the stub is useful to avoid issues associated with charging. The survey and high-resolution (HR) spectra of selected constituent elements were collected at a pass energy of 160, 40 eV, respectively. The XPS scanning parameters include binding energy (BE) range scans—1400 eV − (−5) eV, step size of survey scan—0.5 eV, and the step size for HR scans 0.1 eV. The HR scans for Ba 3d, Fe 2p, Ta 4f, and O 1s core-level XPS data were collected. At least 16 sweeps were recorded to obtain well-resolved HR spectral lines. All of the XPS spectra (survey and HR) were collected under ultrahigh vacuum (UHV—4×10^{-9} torr) conditions. The C 1s peak positioned at 285 eV was used for the charge reference. The CasaXPS V2.3.16 software package was used to analyze the XPS data collected. The Gaussian/Lorentzian (GL(30)) line shape and Shirley background subtraction were used to deconvolute the HR spectra.[46,47]

2.2.3. Fourier Transform Infrared Spectroscopy (FTIR). The infrared transmission measurements were carried out between 400 and 4000 cm^{-1} with a vacuum-based Bruker IFS 66v spectrometer, equipped with deuterated triglycine sulfate (DTGS) detectors, a Ge-coated mylar beam splitter for data acquisition in the far-IR region, and a KBr beam splitter for the mid-IR region. The samples for these studies were prepared in the form of pellets by embedding the material in a polycrystalline CsI matrix. Accumulations of 256 scans at a resolution of 4 cm^{-1} were performed for each spectrum. The data were normalized at each frequency to a vacuum throughput spectrum.

2.2.4. Electrocatalytic Activity Studies. The electrocatalytic activity of BFTO toward the hydrogen evolution reaction and oxygen reduction reaction was evaluated using a three-electrode system. Linear sweep voltammetry (CHI 6273E potentiostat) with a scan rate of 10 mV s^{-1} was conducted using Ag/AgCl reference electrode and graphite as the counter electrode. To prepare the working electrode, a homogeneous mixture of the sample (2 mg/mL) in 1:1 ratio of water and ethanol was prepared. Further, 80 μL of 5 wt % Nafion 117 solution (Sigma-Aldrich) was mixed with the above solution and sonicated well. Twenty microliters of the homogeneous mixture was then drop casted onto a freshly polished glassy carbon working electrode with 3 mm diameter. In the case of HER, the redox properties were studied in the voltage ranging from 0 to −1 V using 0.5 M H_2SO_4 aq. electrolyte. Prior to the HER measurements, the electrolyte solution was purged with argon gas for 20 min. The catalytic activity, determined by ORR, was explored in the solution of an oxygen-rich 0.1 M KOH. The cyclic voltammetry (CV) measurements were carried out in O_2 saturated 0.1 M KOH solution with a scan rate of 10 mV s^{-1}. The potential was converted into RHE scale using the following equation

$$E(\mathrm{RHE}) = E_{\mathrm{Ag/AgCl}} + 0.059\mathrm{pH} + \mathrm{Eo}_{\mathrm{Ag/AgCl}} \quad (1)$$

where $\mathrm{Eo}_{\mathrm{Ag/AgCl}}$ = 0.1976 V and $E_{\mathrm{Ag/AgCl}}$ is the working potential. All of the experiments were performed at room temperature if not stated otherwise.

3. RESULTS AND DISCUSSION

3.1. Electronic Structure and Chemical Valence—X-ray Photoelectron Spectroscopy (XPS). X-ray diffraction analyses revealed the evidence of structural transformations with increasing sintering temperature. The crystal structure details of BFTO compounds have been reported elsewhere.[48] Briefly and for clarity of purpose, the XRD patterns indicate that the samples are stabilized in the perovskite phase without any phase separation even at high temperature. The average crystallite size increases with increasing sintering temperature from ≈24 nm (1200 °C) to ≈80 nm (1350 °C). At 1200 °C, BFTO compounds stabilize in a mixed phase of orthorhombic ($Amm2$) and rhombohedral ($R3m$) components. Structural analyses confirm the stabilization of tetragonal ($P4mm$) and rhombohedral ($R3m$) mixed phase in BFTO compounds with increasing sintering temperature to 1250−1350 °C. As the sintering temperature increases, the fraction of the tetragonal phase gradually decreases whereas that of the rhombohedral phase gradually increases.[48] Electron microscopy data further confirm that the estimated d-spacing values are very well correspond with the constituent phases of the respective BFTO compound.

The XPS survey spectra of BFTO30 compounds are shown in Figure 2. The data shown are for BFTO compounds sintered at different temperatures along with the calcined BFTO sample (1150 °C, see Figure 2a). The XPS survey scans indicate the respective photoemission peaks due to constituent elements (Ba, Fe, Ta, and O) and Auger peaks of Ba and O (Ba MNN & O KLL). The C 1s resulted due to adventitious hydrocarbons on the surface of sample; these hydrocarbons are commonly formed on the surface of the sample when exposed to air while handling. Also, the survey scans confirm that there are no additional peaks and/or no considerable changes in the spectra with increasing sintering temperature. The electronic structure and chemical composition information is further probed by means of the detailed, high-resolution core-level XPS scans of Ba, Fe, Ta, and O. Being a surface-sensitive characterization technique, XPS allowed us to understand the surface chemistry of BFTO compounds and the chemical

https://dx.doi.org/10.1021/acsaem.0c02548
ACS Appl. Energy Mater. 2021, 4, 1313−1322

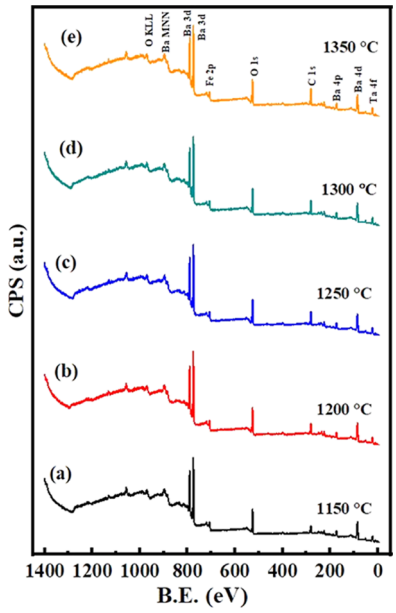

Figure 2. XPS survey scans of BFTO samples. For comparison, the XPS data of BFTO sintered samples (1200, 1250, 1300, and 1350 °C) are shown along with that of the BFTO sample calcined at 1150 °C. The data shown are for BFTO samples processed at temperatures of: (a) 1150, (b) 1200, (c) 1250, (d) 1300, and (e) 1350 °C.

valence state(s) of the constituent elements as discussed below.

The deconvoluted high-resolution XPS spectra of Ba $3d_{5/2}$ in BFTO compounds is shown in Figure 3. The Ba 3d exhibits

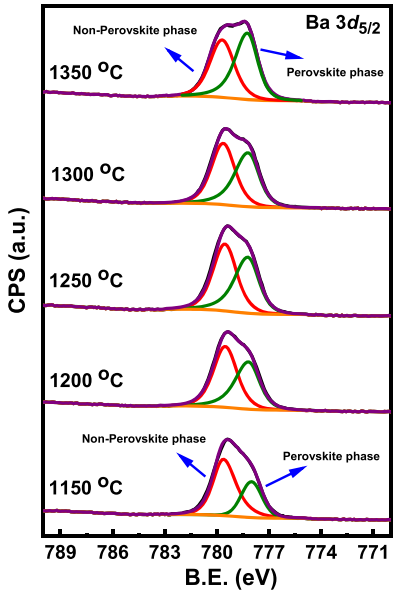

Figure 3. High-resolution core-level XPS data of Ba 3d in BFTO compounds.

two XPS components, which correspond to Ba $3d_{5/2}$ and Ba $3d_{3/2}$ associated with spin−orbit coupling, located at lower and higher binding energies, respectively.[49−51] The high-resolution XPS line of Ba $3d_{5/2}$ (Figure 3) reveals the presence of two clearly visible components, and the deconvolution of peaks using the Gaussian function are also shown in Figure 3. These clearly visible components are fitted mainly with two peaks positioned at 779.50 eV (red) and 778.38 eV (green). These two peaks of Ba $3d_{5/2}$ commonly reported in the literature at lower and higher binding energies, denoted as α and β phases, respectively.[52] The peak at lower binding energy resulted due to Ba atoms in the perovskite phase,[53] whereas the peak at higher binding energy—due to nonperovskite environment such as carbonates, oxides, and oxygen vacancies.[54−56] From the Ba $3d_{5/2}$ spectra, it is evident that the intensity of the perovskite phase gradually increases with increasing sintering temperature, and the intensity reversal of the perovskite and nonperovskite phase is observed at 1350 °C. Such a gradual increase in the intensity of the perovskite phase is due to change in the Ba environment, which is a consequence of structural phase transformation with sintering temperature. Moreover, the decrease in intensity (1350 °C) of the nonperovskite phase with increasing sintering temperature might be due to reduced oxygen vacancies resulted from structural rearrangements.

High-resolution XPS spectra of the Fe 2p region are represented in Figure 4. The high-resolution XPS scan of the

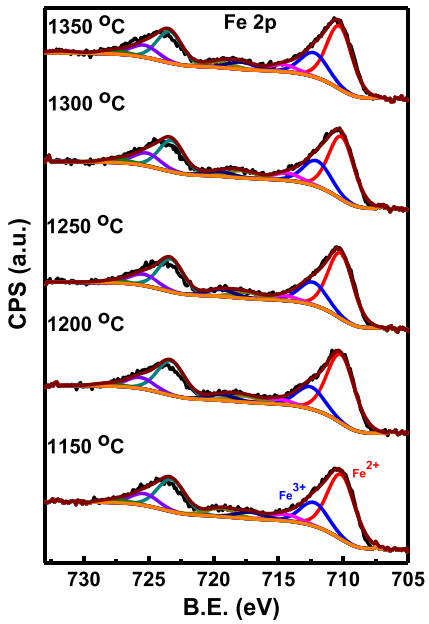

Figure 4. High-resolution core-level XPS data of Fe 2p in BFTO compounds.

Fe 2p region (Figure 4) presents interesting features revealing the characteristic Fe bonding and chemical state in BFTO compounds synthesized at different sintering temperatures. The presence of the characteristic doublet of Fe 2p, i.e., Fe $2p_{3/2}$ and Fe $2p_{1/2}$ peaks, due to spin−orbit splitting[40,57−59] can be seen for all of the BFTO compounds. However, their evolution, in terms of peak shape, etc., is different and interesting to learn about the chemical state and bonding environment of Fe in BFTO. The BE positions of Fe $2p_{3/2}$ and Fe $2p_{1/2}$ peaks are presented in Table 1. It can be noted that the Fe 2p XPS peak exhibits doublet characteristics, which corresponds to Fe $2p_{1/2}$ (~723 eV) and Fe $2p_{3/2}$ (~710 eV), separated by 13.025 eV. The deconvoluted spectra of Fe $2p_{1/2}$ and Fe $2p_{3/2}$ reveal two peaks positioned at ~723, ~725 eV for Fe $2p_{1/2}$ and ~712, ~710 eV for Fe $2p_{3/2}$. These features manifest the coexistence of several valance states[40,58] of Fe, the lower binding energy peaks (723, 710 eV) resulted from Fe^{2+},

https://dx.doi.org/10.1021/acsaem.0c02548
ACS Appl. Energy Mater. 2021, 4, 1313−1322

Table 1. XPS Data of Representative Peaks in BFTO Compounds

	XPS peak (BE) position for respective elements in BFTO compounds									
sintering temperature (°C)	Ba $3d_{5/2}$ (α-phase)	Ba $3d_{3/2}$ (β-phase)	Fe $2p_{3/2}$ (Fe^{3+})	Fe $2p_{3/2}$ (Fe^{2+})	Fe $2p_{1/2}$ (Fe^{3+})	Fe $2p_{1/2}$ (Fe^{3+})	Ta $4f_{7/2}$	Ta $4f_{5/2}$	O 1s (carbonate)	O 1s (oxide)
1200	778.00	779.52	712.69	710.25	725.73	723.29	25.00	26.90	531.10	528.67
1250	778.19	779.57	712.48	710.31	725.54	723.44	25.06	26.95	531.13	528.82
1300	778.23	779.66	712.16	710.26	725.29	723.33	24.89	26.82	530.85	528.84
1350	778.28	780.12	712.41	710.35	725.48	723.41	25.06	26.98	531.03	529.07

and higher binding energy peaks (725, 712 eV) resulted from Fe^{3+}. Moreover, the formation of Fe^{2+} states in Fe sublattice is an evident for oxygen vacancy in Fe-containing compounds. There is no change in the characteristic features of Fe 2p spectra with increasing sintering temperature, and mixed valance state is persistent over the range of studied sintering temperatures. Also, shake-up satellite peak noticed around 718 eV is due to Fe^{3+} in $\alpha-Fe_2O_3$.[58,60,61]

The high-resolution XPS spectra of Ta 4f are displayed in Figure 5. The spectra reveal two clearly visible components

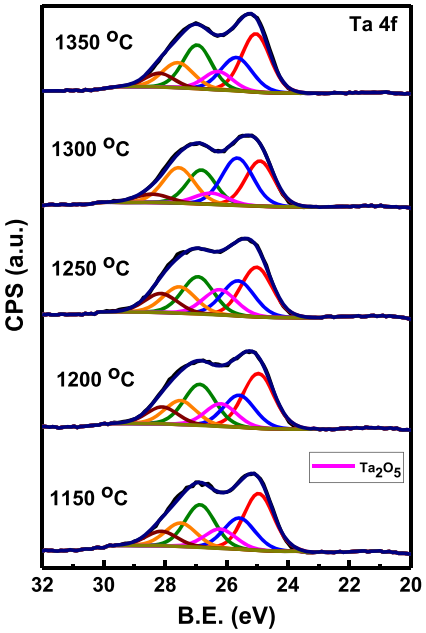

Figure 5. High-resolution core-level XPS data of Ta 4f in BFTO compounds.

corresponding to Ta $4f_{7/2}$ and Ta $4f_{5/2}$ positioned at ≈25.2 and 27.0 eV, respectively. The BE positions of respective peaks are presented in Table 1. The asymmetry and broadening of XPS lines evident for Ta atoms are surrounded by different chemical environments.[62] The deconvoluted spectra show complex Ta $4f_{7/2}$ and Ta $4f_{5/2}$ peaks containing four additional peaks, two located at lower binding energies with respect to Ta $4f_{7/2}$ and other two located at lower binding energies with respect to Ta $4f_{5/2}$. The main components are the resultant of Ta atoms in the perovskite phase with Ta^{5+} state.[63,64] The additional peaks correspond to tantalum suboxide.[63,64]

The high-resolution XPS spectra of O 1s core level are presented in Figure 6. At very first glance, the spectra indicate two clearly visible peaks and a shoulder at higher binding energy. The deconvoluted spectra exhibit multiple peaks positioned (Table 1) at ∼529 eV (blue), ∼530 eV (green), ∼531 eV (red), ∼532 eV (orange), and ∼533 eV (violet). A

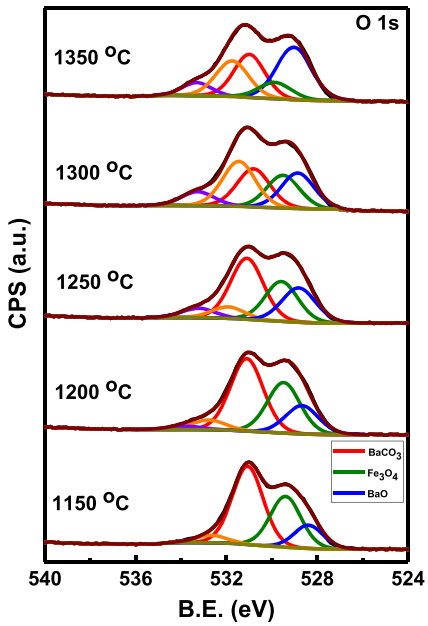

Figure 6. Detailed XPS spectra of O 1s core level in BFTO compounds.

distinct peak (blue) at ∼529 eV corresponds to oxygen in the metal oxide framework of the perovskite lattice.[65] The intensity of this peak gradually increases with increasing sintering temperature, and the increment in intensity is attributed to change in the chemical environment due to structural transformation. Another peak located at ∼531 eV (red) corresponds to metal carbonate; the intensity of metal carbonate gradually decreases with increasing sintering temperature. The peaks located at 530 eV (green), ∼532 eV(orange), and ∼533 eV (violet) are attributed to oxygen bonded to carbon and surface hydroxyl groups.[65,66]

3.2. Chemical Bonding—Fourier Transform Infrared Spectroscopy (FTIR). To validate structural transformations and chemical bonding and also to follow relative changes as a function of sintering temperature, detailed FTIR analysis was performed on BFTO samples synthesized at different T_s. The FTIR spectra of BFTO compounds are shown in Figure 7. For comparison, the FTIR data of precursor materials are also shown in Figure 7b. The FTIR spectra of BFTO compounds (Figure 7a) can be conveniently discussed by comparing the data with that of intrinsic $BaTiO_3$ (BT) perovskite. It has been reported widely in the literature that, for intrinsic BT compound, the FTIR spectra exhibit two strong peaks around 554 and 520 cm^{-1}.[67−70] The former is usually ascribed to TiO_6 stretching vibration that is connected to Ba ion, while the latter is due to TiO stretching vibration along the polar axis of spontaneous polarization in tetragonal BT.[67,68] Similarly, a Ti−O bond or TiO_4 tetrahedral band appears at around 630−700

https://dx.doi.org/10.1021/acsaem.0c02548
ACS Appl. Energy Mater. 2021, 4, 1313−1322

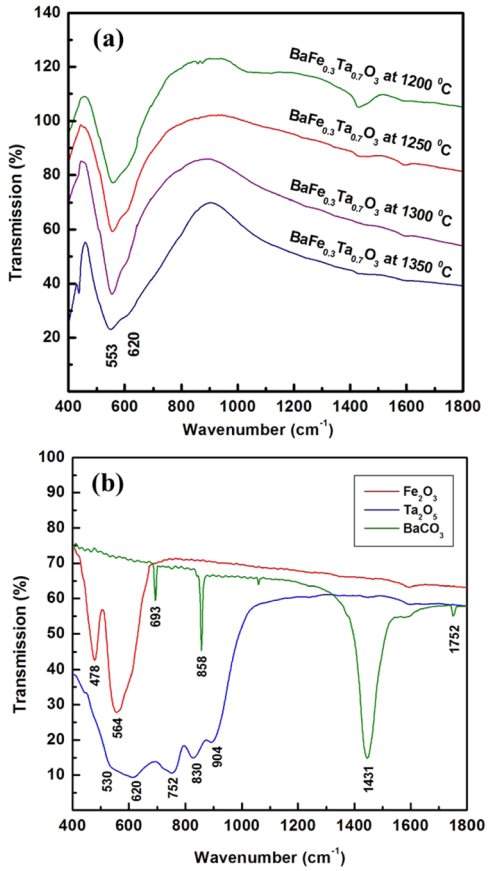

Figure 7. FTIR spectra of BFTO samples sintered at different temperatures. (a) BFTO samples sintered at T_s = 1200−1350 °C; (b) FTIR data of precursor oxides.

cm^{-1} in the FTIR spectra.[68,69] Thus, the FTIR absorption band observed at 553 cm^{-1} for BFTO samples can be ascribed to MO_6 stretching vibration that is connected to Ba ion. The presence of this band can be noted for BFTO samples sintered at variable temperatures. This observation indicates that the chemical bonding environment of MO_6 octahedra in these doped BFTO samples is well maintained, and it is as expected for BT-based perovskite compounds. The absorption band located at 620 cm^{-1} can be ascribed to the stretching mode of M−O (Ta−O) bond vibration. However, this absorption band is located at 605 cm^{-1} in pure BT and is associated with the stretching mode of Ti−O bond vibration.[67,70] The absorption band appeared at a slightly higher wavenumber in the BFTO compound reflects the effect of Ta doping. Note that, when Ta is doped to form a BFTO compound, Ta^{5+} ions replace the position of Ti^{4+} resulting in the absorption band shift to higher wavenumber due to a smaller radius of Ta^{5+} ion. Therefore, Ta doping induces slight distortion in the lattice parameter and chemical bonding. In this case, the positive shift of the absorption band indicates the reduction in bond energy, i.e., a difference in the Ti−O versus Ta−O chemical bonds. Such variation in bond energy or strength and associated absorption band shift in FTIR is reported in Ta-doped PZT. It was reported that, when Ta is added, Ta^{5+} ions affect the Coulomb interaction among the ions leading to a positive shift in the absorption band. Furthermore, the magnitude of the positive shift was shown to directly correlate with the Ta content or the amount of Ta^{5+} ions replacing for Zr^{4+} or Ti^{4+} ions. The observed FTIR absorption bands and the implications are corroborated with the XRD data reported elsewhere.[48]

The chemical quality of the BFTO compounds synthesized can be understood if we consider the absorption bands in the higher wavelength (>1000 cm^{-1}) region. It has been widely reported for intrinsic and doped BT compounds that the broad absorption bands in the range of bands 1220−1760 cm^{-1} are

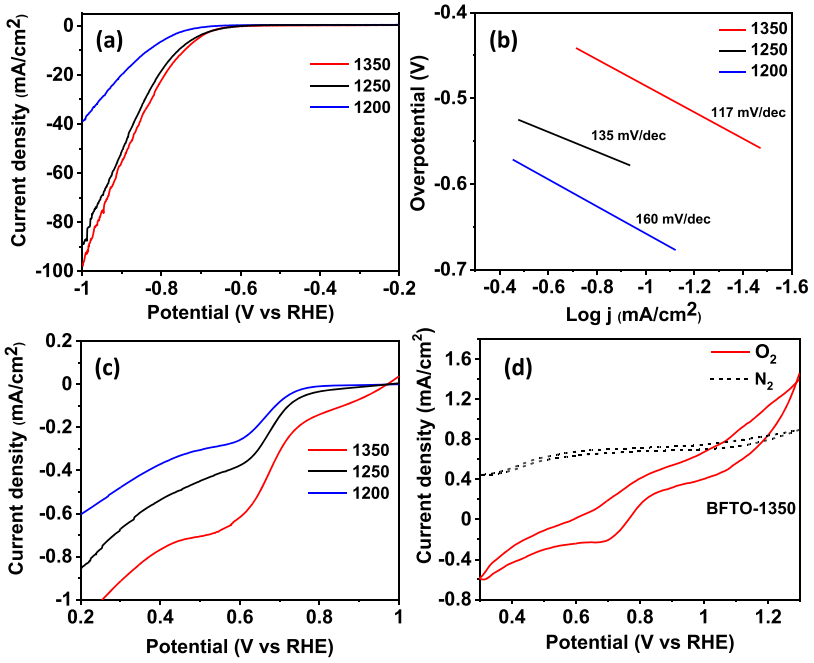

Figure 8. (a) LSV of BFTO samples at different temperatures in 0.5 M H_2SO_4 solution at a scan rate of 10 mV s^{-1}, (b) Tafel plots of as-synthesized BFTO at different temperatures, (c) LSVs of BFTO samples at different temperatures in O_2-saturated 0.1 M KOH solution at a scan rate of 10 mV s^{-1}, and (d) CV of BFTO-1350 °C in O_2- and N_2-saturated solutions.

https://dx.doi.org/10.1021/acsaem.0c02548
ACS Appl. Energy Mater. 2021, 4, 1313−1322

typically present in the FTIR spectra due to the presence of carbon (C) bonded with hydrogen (H) or oxygen (O) or nitrogen (N).[68−70] Such bands are fully absent in these BFTO compounds except the band at 1445 cm^{-1} in BFTO sintered at a lower temperature (1200 °C). This may be due to the presence of carbonates originated in the solid-phase formation and incomplete digestion of the respective chemicals used to prepare BFTO materials.[68] On the other hand, the absorption bands located at about ∼2900−3000 cm^{-1} and related to hydroxyl groups are not at all seen in any of the BFTO materials synthesized at variable T_s. This observation is an indication of the fact that such molecules that are usually present in intrinsic or doped BT materials synthesized by wet chemical methods are not present in these BFTO samples, which is primarily due to the effect of processing at higher temperatures.

3.3. Electrocatalytic Activity. The presence of Fe and Ba with documented ability as electrocatalysts encouraged us to evaluate its electrocatalytic efficacy toward HER and ORR. The electrocatalytic water splitting, especially HER performance of the as-synthesized BFTO samples, was evaluated using linear sweep voltammetry (Figure 8a,b). Though all of the samples demonstrated appreciable electrocatalytic properties (as illustrated by the significant current densities), a general decrease in activity (increase in onset potential) was observed as the sintering temperature is decreased. For example, BFTO-1350 °C showed an onset potential of −0.690 V and an overpotential of −0.790 V (at j = 20 mA cm^{-2}) indicating its significant electrocatalytic performance toward HER. However, samples prepared at 1250 °C (BFTO-1250 °C) and 1200 °C (BFTO-1200 °C) illustrated comparable (but slightly lower) activity with an onset potential of −0.705 V (an overpotential of −0.800 V at j = 20 mA cm^{-2}) and −0.728 V (an overpotential of −0.900 V at j = 20 mA cm^{-2}), respectively. The Tafel slope of the amperometry response for a catalyst-modified electrode is an inherent property indicative of the rate-limiting step for HER. The linear portions of the Tafel plots are fitted to the Tafel equation ($\eta = b \log j + a$, where j is the current density and b is the Tafel slope) to obtain a slope of 117 mV dec^{-1} for BFTO-1350 °C, 135 mV dec^{-1} for BFTO-1250 °C, and 160 mV dec^{-1} for BFTO-1200 °C. From Butler−Volmer kinetics, it can be deduced that the discharge reaction is the rate-limiting step in the case of BFTO-1350 °C. The lower onset potential and Tafel slope, in combination with a higher current density, indicate the superiority of BFTO samples treated at higher temperature toward HER.

Electrochemical oxygen reduction reaction plays an important role in sustainable energy conversion and storage devices such as fuel cells and metal−air batteries. The composites from nonprecious metal catalysts such as Ba, Fe, and Ta attracted broad research interest in recent years because of their relatively high ORR activity.[71−75] Hence, we investigated the ORR activity of the as-synthesized Fe, Ta co-doped perovskite structured oxides (Figure 8c,d). Similar to HER, the highest activity was shown by BFTO-1350 °C with an onset potential of 0.73 V vs RHE. The tilted plateau between 0.2 and 0.4 V shown by the BFTO samples could be because of the transition of control from kinetics to diffusion. The cyclic voltammogram shown in Figure 8d reveals the substantial reduction process at about 0.7 V in the presence of oxygen, whereas no obvious response is observed at the same potential range under nitrogen, confirming the catalytic activity of BFTO-1350 °C toward ORR. Hence, our study indicates the potential bifunctional catalytic activity of BFTO-1350 °C toward HER and ORR. The observed enhancement in electrochemical activity for HER and ORR with an increase in sintering temperature is attributed to the improved structural quality resulting in higher electrochemical active centers.

4. SUMMARY AND CONCLUSIONS

Detailed studies were performed to understand the electronic structure and electrocatalytic activity of $Ba(Fe_{0.7}Ta_{0.3})O_{3-\delta}$ (BFTO) compounds synthesized by the conventional high-temperature solid-state ceramic reaction method. The chemical environment of Fe and Ta cations in BFTO is strongly influenced by the sintering temperature and resulting structural quality of the compounds. A deeper analysis of Ba 3d, Fe 2p, Ta 4f, and O 1s core-level XPS data reveal the local structure, electronic charge distribution, and chemical bonding environment of Ba, Fe, Ta cations and their chemical valence states in the BFTO compounds. The chemical bonding analysis made using FTIR spectroscopy indicates the presence of absorption bands that are exclusively due to MO_6 stretching vibration that is connected to Ba ion as well as stretching of M−O bonds in BFTO compounds. The presence of only these absorption bands and the absence of any of those absorption bands related to C−H, C−O, and C−N bonds that are typically present in compounds synthesized by wet chemical methods clearly indicate the chemical quality of BFTO materials. The resultant BFTO catalysts exhibited significant electrocatalytic activities for both hydrogen evolution and oxygen reduction reactions. BFTO sintered at 1350 °C showed the best electrochemical catalytic activity for HER with an onset potential of −0.690 V vs RHE and an overpotential of −0.790 V vs RHE (at j = 20 mA cm^{-2}), indicating its significant electrocatalytic performance toward HER. In the case of ORR, the highest activity was shown by BFTO-1350 °C with an onset potential of 0.73 V vs RHE. The electrocatalytic activity enhancement noted in BFTO compounds with increasing sintering temperature is attributed to the improved structural quality and electronic structure. The present work may contribute to the design and development of $Ba(Fe_{0.7}Ta_{0.3})O_{3-\delta}$ materials for high-temperature oxygen sensors and electrocatalytic converters.

AUTHOR INFORMATION

Corresponding Author

C. V. Ramana − *Center for Advanced Materials Research (CMR), University of Texas at El Paso, El Paso, Texas 79968, United States;* orcid.org/0000-0002-5286-3065; Email: rvchintalapalle@utep.edu

Authors

Mallesham Bandi − *Center for Advanced Materials Research (CMR), University of Texas at El Paso, El Paso, Texas 79968, United States;* orcid.org/0000-0002-7875-3518

Aruna N Nair − *Department of Chemistry and Biochemistry, University of Texas at El Paso, El Paso, Texas 79968, United States*

Felicia S. Manciu − *Department of Physics, El Paso, Texas 79968, United States*

Sreeprasad Sreenivasan − *Department of Chemistry and Biochemistry, University of Texas at El Paso, El Paso, Texas 79968, United States;* orcid.org/0000-0002-5728-0512

Vaithiyalingam Shutthanandan − *Environmental Molecular Sciences Laboratory (EMSL), Pacific Northwest National*

https://dx.doi.org/10.1021/acsaem.0c02548
ACS Appl. Energy Mater. 2021, 4, 1313−1322

Laboratory (PNNL), Richland, Washington 99352, United States; orcid.org/0000-0003-2957-7535

Complete contact information is available at: https://pubs.acs.org/10.1021/acsaem.0c02548

Notes

The authors declare no competing financial interest.

■ ACKNOWLEDGMENTS

The authors acknowledge, with pleasure, support from the National Science Foundation (NSF) with NSF-PREM grant #DMR-1827745. In addition, one of the authors (S.S.) would like to acknowledge the support through UTEP start-up, UT STARs, and URI funding. The authors sincerely acknowledge the technical assistance offered by Dr. Roy Swadipta for recording the survey and detailed core-level XPS spectra of all of the BFTO compounds. A portion of the research (XPS studies) was performed using Environmental Molecular Sciences Laboratory (EMSL), a national scientific user facility sponsored by the Department of Energy's Office of Biological and Environmental Research and located at Pacific Northwest National Laboratory.

■ REFERENCES

(1) Hong, W. T.; Risch, M.; Stoerzinger, K. A.; Grimaud, A.; Suntivich, J.; Shao-Horn, Y. Toward the Rational Design of Non-Precious Transition Metal Oxides for Oxygen Electrocatalysis. *Energy Environ. Sci.* **2015**, *8*, 1404−1427.

(2) el Hadri, A.; Gómez-Recio, I.; Río, E. D.; Hernández-Garrido, J. C.; Cortés-Gil, R.; Hernando, M.; Varela, A. U.; Gutiérrez-Alonso, A. N.; Parras, M.; Delgado, J. J.; et al. Critical Influence of Redox Pretreatments on the Co Oxidation Activity of $BaFeO_{3-\delta}$ Perovskites: An in-Depth Atomic-Scale Analysis by Aberration-Corrected and in Situ Diffraction Techniques. *ACS Catal.* **2017**, *7*, 8653−8663.

(3) Seo, M. H.; Park, H. W.; Lee, D. U.; Park, M. G.; Chen, Z. Design of Highly Active Perovskite Oxides for Oxygen Evolution Reaction by Combining Experimental and Ab Initio Studies. *ACS Catal.* **2015**, *5*, 4337−4344.

(4) May, K. J.; Carlton, C. E.; Stoerzinger, K. A.; Risch, M.; Suntivich, J.; Lee, Y.-L.; Grimaud, A.; Shao-Horn, Y. Influence of Oxygen Evolution During Water Oxidation on the Surface of Perovskite Oxide Catalysts. *J. Phys. Chem. Lett.* **2012**, *3*, 3264−3270.

(5) Xu, X.; Zhong, Y.; Shao, Z. Double Perovskites in Catalysis, Electrocatalysis, and Photo (Electro)Catalysis. *Trends Chem.* **2019**, *1*, 410−424.

(6) Li, M.; Pietrowski, M. J.; De Souza, R. A.; Zhang, H.; Reaney, I. M.; Cook, S. N.; Kilner, J. A.; Sinclair, D. C. A Family of Oxide Ion Conductors Based on the Ferroelectric Perovskite $Na_{0.5}Bi_{0.5}TiO_3$. *Nat. Mater.* **2014**, *13*, 31−35.

(7) She, S.; Yu, J.; Tang, W.; Zhu, Y.; Chen, Y.; Sunarso, J.; Zhou, W.; Shao, Z. Systematic Study of Oxygen Evolution Activity and Stability on $La_{1-x}Sr_xFeO_{3-\delta}$ Perovskite Electrocatalysts in Alkaline Media. *ACS Appl. Mater. Interfaces* **2018**, *10*, 11715−11721.

(8) Tripkovic, V.; Hansen, H. A.; Garcia-Lastra, J. M.; Vegge, T. Comparative DFT+ U and Hse Study of the Oxygen Evolution Electrocatalysis on Perovskite Oxides. *J. Phys. Chem. C* **2018**, *122*, 1135−1147.

(9) Di Tommaso, S.; Giannici, F.; Mossuto Marculescu, A.; Martorana, A.; Adamo, C.; Labat, F. Toward Tailorable Surfaces: A Combined Theoretical and Experimental Study of Lanthanum Niobate Layered Perovskites. *J. Chem. Phys.* **2014**, *141*, No. 024704.

(10) Chen, D.; Chen, C.; Baiyee, Z. M.; Shao, Z.; Ciucci, F. Nonstoichiometric Oxides as Low-Cost and Highly-Efficient Oxygen Reduction/Evolution Catalysts for Low-Temperature Electrochemical Devices. *Chem. Rev.* **2015**, *115*, 9869−9921.

(11) Benedek, N. A.; Fennie, C. J. Why Are There So Few Perovskite Ferroelectrics? *J. Phys. Chem. C* **2013**, *117*, 13339−13349.

(12) Bowen, C. R.; Kim, H.; Weaver, P.; Dunn, S. Piezoelectric and Ferroelectric Materials and Structures for Energy Harvesting Applications. *Energy Environ. Sci.* **2014**, *7*, 25−44.

(13) Ju, L.; Sabergharesou, T.; Stamplecoskie, K. G.; Hegde, M.; Wang, T.; Combe, N. A.; Wu, H.; Radovanovic, P. V. Interplay between Size, Composition, and Phase Transition of Nanocrystalline Cr^{3+}-Doped $BaTiO_3$ as a Path to Multiferroism in Perovskite-Type Oxides. *J. Am. Chem. Soc.* **2012**, *134*, 1136−1146.

(14) Xu, X.; Pan, Y.; Zhong, Y.; Ran, R.; Shao, Z. Ruddlesden−Popper Perovskites in Electrocatalysis. *Mater. Horiz.* **2020**, *7*, 2519−2565.

(15) Srilakshmi, C.; Saraf, R.; Prashanth, V.; Rao, G. M.; Shivakumara, C. Structure and Catalytic Activity of Cr-Doped $BaTiO_3$ Nanocatalysts Synthesized by Conventional Oxalate and Microwave Assisted Hydrothermal Methods. *Inorg. Chem.* **2016**, *55*, 4795−4805.

(16) Srilakshmi, C.; Rao, G. M.; Saraf, R. Effect of the Nature of a Transition Metal Dopant in Batio 3 Perovskite on the Catalytic Reduction of Nitrobenzene. *RSC Adv.* **2015**, *5*, 45965−45973.

(17) Upadhyay, S.; Shrivastava, J.; Solanki, A.; Choudhary, S.; Sharma, V.; Kumar, P.; Singh, N.; Satsangi, V. R.; Shrivastav, R.; Waghmare, U. V.; Dass, S. Enhanced Photoelectrochemical Response of $BaTiO_3$ with Fe Doping: Experiments and First-Principles Analysis. *J. Phys. Chem. C* **2011**, *115*, 24373−24380.

(18) Keswani, B. C.; Devan, R. S.; Kambale, R. C.; James, A. R.; Manandhar, S.; Kolekar, Y. D.; Ramana, C. V. Correlation between Structural, Magnetic and Ferroelectric Properties of Fe-Doped (Ba-Ca)TiO_3 Lead-free Piezoelectric. *J. Alloys Compd.* **2017**, *712*, 320−333.

(19) Keswani, B. C.; Patil, S.; James, A.; Kolekar, Y.; Ramana, C. V. Correlation between Structural, Ferroelectric, Piezoelectric and Dielectric Properties of $Ba_{0.7}Ca_{0.3}TiO_{3-X}BaTi_{0.8}Zr_{0.2}O_3$ (X = 0.45, 0.55) Ceramics. *Ceramics Int.* **2018**, *44*, 20921−20928.

(20) Keswani, B. C.; Saraf, D.; Patil, S.; Kshirsagar, A.; James, A.; Kolekar, Y.; Ramana, C. V. Role of α-Site Ca and B-Site Zr Substitution in $BaTiO_3$ Lead-Free Compounds: Combined Experimental and First Principles Density Functional Theoretical Studies. *J. Appl. Phys.* **2018**, *123*, No. 204104.

(21) Argirusis, C.; Jomard, F.; Wagner, S. F.; Menesklou, W.; Ivers-Tiffée, E. Study of the Oxygen Incorporation and Diffusion in $Sr(Ti_{0.65}Fe_{0.35})O_3$ Ceramics. *Solid State Ionics* **2011**, *192*, 9−11.

(22) Sahner, K.; Straub, J.; Moos, R. Cuprate-ferrate Compositions for Temperature Independent Resistive Oxygen Sensors. *J. Electroceram.* **2006**, *16*, 179−186.

(23) Fergus, J. W. Perovskite Oxides for Semiconductor-Based Gas Sensors. *Sens. Actuators, B* **2007**, *123*, 1169−1179.

(24) Zhou, H.; Goodenough, J. B. Polaron Morphologies in $SrFe_{1-x}Ti_xO_{3-\delta}$. *J. Solid State Chem.* **2004**, *177*, 1952−1957.

(25) Wang, X.; Wu, J.; Xiao, D.; Zhu, J.; Cheng, X.; Zheng, T.; Zhang, B.; Lou, X.; Wang, X. Giant Piezoelectricity in Potassium−Sodium Niobate Lead-Free Ceramics. *J. Am. Chem. Soc.* **2014**, *136*, 2905−2910.

(26) Panda, P. Environmental Friendly Lead-Free Piezoelectric Materials. *J. Mater. Sci.* **2009**, *44*, 5049−5062.

(27) Ishihara, T. Inorganic Perovoskite Oxides. In *Springer Handbook of Electronic and Photonic Materials*; Kasap, S.; Capper, P., Eds.; Springer, 2017.

(28) He, B.; Tan, K.; Gong, Y.; Wang, R.; Wang, H.; Zhao, L. Coupling Amorphous Cobalt Hydroxide Nanoflakes on Sr2Fe1.5-Mo0.5O5pδ Perovskite Nanofibers to Induce Bifunctionality for Water Splitting. *Nanoscale* **2020**, *12*, 9048−9057.

(29) Bektas, M.; Schönauer-Kamin, D.; Hagen, G.; Mergner, A.; Bojer, C.; Lippert, S.; Milius, W.; Breu, J.; Moos, R. $BaFe_{1-X}Ta_xO_{3-\delta}$−a Material for Temperature Independent Resistive Oxygen Sensors. *Sens. Actuators, B* **2014**, *190*, 208−213.

(30) Bektas, M.; Stöcker, T.; Mergner, A.; Hagen, G.; Moos, R. Combined Resistive and Thermoelectric Oxygen Sensor with Almost

Temperature-Independent Characteristics. *J. Sens. Sens. Syst.* **2018**, *7*, 289.
(31) Rothschild, A.; Litzelman, S. J.; Tuller, H. L.; Menesklou, W.; Schneider, T.; Ivers-Tiffée, E. Temperature-Independent Resistive Oxygen Sensors Based on $SrTi_{1-X}Fe_xO_{3-\delta}$ Solid Solutions. *Sens. Actuators, B* **2005**, *108*, 223−230.
(32) Chow, C. L.; Ang, W. C.; Tse, M. S.; Tan, O. K. Oxygen-sensing Property of Sol-Gel-Derived $SrTi_{1-x}Fe_xO_{3-\delta}$ Thin Films with Different Iron Concentrations (x = 0.2−0.8). *Thin Solid Films* **2013**, *542*, 393−398.
(33) Wang, D.; Ye, J.; Kako, T.; Kimura, T. Photophysical and Photocatalytic Properties of $SrTiO_3$ Doped with Cr Cations on Different Sites. *J. Phys. Chem. B* **2006**, *110*, 15824−15830.
(34) Kato, H.; Kudo, A. Visible-Light-Response and Photocatalytic Activities of TiO_2 and $SrTiO_3$ Photocatalysts Codoped with Antimony and Chromium. *J. Phys. Chem. B* **2002**, *106*, 5029−5034.
(35) Ishii, T.; Kato, H.; Kudo, A. H_2 Evolution from an Aqueous Methanol Solution on $SrTiO_3$ Photocatalysts Codoped with Chromium and Tantalum Ions under Visible Light Irradiation. *J. Photochem. Photobiol., A* **2004**, *163*, 181−186.
(36) Niishiro, R.; Kato, H.; Kudo, A. Nickel and either Tantalum or Niobium-codoped TiO_2 and $SrTiO_3$ Photocatalysts with Visible-light Response for H_2 or O_2 Evolution from Aqueous Solutions. *Phys. Chem. Chem. Phys.* **2005**, *7*, 2241−2245.
(37) She, S.; Yu, J.; Tang, W.; Zhu, Y.; Chen, Y.; Sunarso, J.; Zhou, W.; Shao, Z. Systematic study of oxygen evolution activity and stability on La1-xSrxFeO3-δ perovskite electrocatalysts in alkaline media. *ACS Appl. Mater. Interfaces* **2018**, *10*, 11715−11721.
(38) Xu, X.; Chen, Y.; Zhou, W.; Zhong, Y.; Guan, D.; Shao, Z. Earth abundant silicon for facilitating water oxidation over iron based perovskite electrocatalyst. *Adv. Mater. Interfaces* **2018**, *5*, 1701693−1701699.
(39) Kim, B. J.; Fabbri, E.; Abbott, D. F.; Cheng, X.; Clark, A. H.; Nachtegaal, M.; Borlaf, M.; Castelli, I. E.; Graule, T.; Schmidt, T. J. Functional Role of Fe doping in Co-based perovskite oxide catalysts for oxygen evolution reaction. *J. Am. Chem. Soc.* **2019**, *141*, 5231−5240.
(40) Mallesham, B.; Roy, S.; Bose, S.; Nair, A. N.; Sreenivasan, S.; Shutthanandan, V.; Ramana, C. V. Crystal Chemistry, Band-Gap Red Shift, and Electrocatalytic Activity of Iron-Doped Gallium Oxide Ceramics. *ACS Omega* **2020**, *5*, 104−112.
(41) Xu, X.; Chen, Y.; Zhou, W.; Zhu, Z.; Su, C.; Liu, M.; Shao, Z. A Perovskite Electrocatalyst for Efficient Hydrogen Evolution Reaction. *Adv. Mater.* **2016**, *28*, 6442−6448.
(42) Xu, X.; Pan, Y.; Zhong, Y.; Ge, L.; Jiang, S. P.; Shao, Z. From Scheelite $BaMoO_4$ to Perovskite $BaMoO_3$: Enhanced Electrocatalysis Toward the Hydrogen Evolution in Alkaline Media. *Composites, Part B* **2020**, *198*, No. 108214.
(43) Goswami, C.; Hazarika, K. K.; Bharali, P. Transition metal oxide nanocatalysts for oxygen reduction reaction. *Mater. Sci. Energy Technol.* **2018**, *1*, 117−128.
(44) Zhong, L.; Li, S. Unconventional Oxygen Reduction Reaction Mechanism and Scaling Relation on Single-Atom Catalysts. *ACS Catal.* **2020**, *10*, 4313−4318.
(45) Gewirth, A. A.; Varnell, J. A.; DiAscro, A. M. Nonprecious Metal Catalysts for Oxygen Reduction in Heterogeneous Aqueous Systems. *Chem. Rev.* **2018**, *118*, 2313−2339.
(46) Fairley, N.; Carrick, A. *Recipes for XPS Data Processing*; Acolyte Science, 2005.
(47) *NIST X-ray Photoelectron Spectroscopy Database*; NIST Standard Reference Database Number 20, NIST: Gaithersburg, MD, 20899, 2000.
(48) Mallesham, B.; Zade, V.; Rubio, A.; Tan, S.; Panat, R.; Ramana, C. V. Unravelling the Sintering Temperature-Induced Phase Transformations in $Ba(Fe_{0.7}Ta_{0.3})O_{3-\delta}$ Ceramics. *Ceramics Int.* **2020**, *46*, 23257−23261.
(49) Alema, F.; Pokhodnya, K. Dielectric Properties of $BaMg_{1/3}Nb_{2/3}O_3$ Doped $Ba_{0.45}Sr_{0.55}TiO_3$ Thin Films for Tunable Microwave Applications. *J. Adv. Dielectr.* **2015**, *05*, No. 1550030.
(50) Atuchin, V. V.; Kesler, V. G.; Kokh, A. E.; Pokrovsky, L. D. X-ray Photoelectron Spectroscopy Study of β-BaB_2O_4 Optical Surface. *Appl. Surf. Sci.* **2004**, *223*, 352−360.
(51) Atuchin, V. V.; Kesler, V. G.; Sapozhnikov, V. K.; Yakovenchuk, V. N. X-ray Photoelectron Spectrometry and Binding Energies of Be 1s and O 1s Core Levels in Clinobarylite, $BaBe_2Si_2O_7$, from Khibiny Massif, Kola peninsula. *Mater. Charact.* **2008**, *59*, 1329−1334.
(52) Datta, K.; Roleder, K.; Thomas, P. Enhanced Tetragonality in Lead-Free Piezoelectric $(1-X)BaTiO_{3-X}Na_{1/2}Bi_{1/2}TiO_3$ Solid Solutions Where X = 0.05−0.40. *J. Appl. Phys.* **2009**, *106*, No. 123512.
(53) Baniecki, J.; Ishii, M.; Kurihara, K.; Yamanaka, K.; Yano, T.; Shinozaki, K.; Imada, T.; Kobayashi, Y. Chemisorption of Water and Carbon Dioxide on Nanostructured $BaTiO_3$−$SrTiO_3$ (001) Surfaces. *J. Appl. Phys.* **2009**, *106*, No. 054109.
(54) Miot, C.; Husson, E.; Proust, C.; Erre, R.; Coutures, J. X-Ray Photoelectron Spectroscopy Characterization of Barium Titanate Ceramics Prepared by the Citric Route. Residual Carbon Study. *J. Mater. Res.* **1997**, *12*, 2388−2392.
(55) Fujisaki, Y.; Shimamoto, Y.; Matsui, Y. Analysis of Decomposed Layer Appearing on the Surface of Barium Strontium Titanate. *Jpn. J. Appl. Phys.* **1999**, *38*, L52.
(56) Essary, C.; Ramani, K.; Craciun, V.; Singh, R. Improvement in Electrical Properties and Thermal Stability of Low-Temperature-Processed Hf−Al−O Gate Dielectrics. *Appl. Phys. Lett.* **2006**, *88*, No. 182902.
(57) Roy, S.; Mallesham, B.; Zade, V. B.; Martinez, A.; Shutthanandan, V.; Thevuthasan, S.; Ramana, C. V. Correlation between Structure, Chemistry, and Dielectric Properties of Iron-Doped Gallium Oxide $(Ga_{2-X}Fe_XO_3)$. *J. Phys. Chem. C* **2018**, *122*, 27597−27607.
(58) Grosvenor, A. P.; Cavell, R. G.; Mar, A. Next-Nearest Neighbour Contributions to P $2p_{3/2}$ X-Ray Photoelectron Binding Energy Shifts of Mixed Transition-Metal Phosphides M1− Xm′ Xp with the Mnp-Type Structure. *J. Solid State Chem.* **2007**, *180*, 2702−2712.
(59) Atuchin, V. V.; Vinnik, D. A.; Gavrilova, T. A.; Gudkova, S. A.; Isaenko, L. I.; Xingxing, J.; Pokrovsky, L. D.; Prosvirin, I. P.; Mashkovtseva, L. S.; Zheshuai, L. Flux Crystal Growth and the Electronic Structure of $BaFe_{12}O_{19}$ Hexaferrite. *J. Phys. Chem. C* **2016**, *120*, 5114−5123.
(60) Kraushofer, F.; Jakub, Z.; Bichler, M.; Hulva, J.; Drmota, P.; Weinold, M.; Schmid, M.; Setvin, M.; Diebold, U.; Blaha, P.; Parkinson, G. S. Atomic-Scale Structure of the Hematite α-Fe_2O_3 $(1\bar{1}02)$ "R-Cut" Surface. *J. Phys. Chem. C* **2018**, *122*, 1657−1669.
(61) Hu, X.; Yu, J. C.; Gong, J.; Li, Q.; Li, G. α-Fe_2O_3 Nanorings Prepared by a Microwave-Assisted Hydrothermal Process and Their Sensing Properties. *Adv. Mater.* **2007**, *19*, 2324−2329.
(62) Jones, D. R.; Gomez, V.; Bear, J. C.; Rome, B.; Mazzali, F.; McGettrick, J. D.; Lewis, A. R.; Margadonna, S.; Al-Masry, W. A.; Dunnill, C. W. Active Removal of Waste Dye Pollutants using Ta_3N_5/$W_{18}O_{49}$ Nanocomposite Fibres. *Sci. Rep.* **2017**, *7*, No. 4090.
(63) Kerrec, O.; Devilliers, D.; Groult, H.; Marcus, P. Study of Dry and Electrogenerated Ta_2O_5 and Ta/Ta_2O_5/Pt Structures by XPS. *Mater. Sci. Eng., B* **1998**, *55*, 134−142.
(64) Imai, Y.; Watanabe, A.; Mukaida, M.; Osato, K.; Tsunoda, T.; Kameyama, T.; Fukuda, K. Stoichiometry of Tantalum Oxide Films Prepared by KrF Excimer Laser-Induced Chemical Vapor Deposition. *Thin Solid Films* **1995**, *261*, 76−82.
(65) Dupin, J.-C.; Gonbeau, D.; Vinatier, P.; Levasseur, A. Systematic XPS Studies of Metal Oxides, Hydroxides and Peroxides. *Phys. Chem. Chem. Phys.* **2000**, *2*, 1319−1324.
(66) Perron, H.; Vandenborre, J.; Domain, C.; Drot, R.; Roques, J.; Simoni, E.; Ehrhardt, J.-J.; Catalette, H. Combined Investigation of Water Sorption on TiO_2 Rutile (1 1 0) Single Crystal Face: XPS Vs. Periodic Dft. *Surf. Sci.* **2007**, *601*, 518−527.
(67) Shiratori, Y.; Pithan, C.; Dornseiffer, J.; Waser, R. Raman Scattering Studies on Nanocrystalline $BaTiOo_3$ Part I - Isolated Particles and Aggregates. *J. Raman Spectrosc.* **2007**, *38*, 1288−1299.

https://dx.doi.org/10.1021/acsaem.0c02548
ACS Appl. Energy Mater. 2021, 4, 1313−1322

(68) Busca, G.; Buscaglia, V.; Leoni, M.; Nanni, P. Solid-State and Surface Spectroscopic Characterization of $BaTiO_3$ Fine Powders. *Chem. Mater.* **1994**, *6*, 955−961.
(69) Ray, S.; Kolen'ko, Y. V.; Kovnir, K. A.; Lebedev, O. I.; Turner, S.; Chakraborty, T.; Erni, R.; Watanabe, T.; Tendeloo, G. A.; Yoshimura, M.; Itoh, M. Defect Controlled Room Temperature Ferromagnetism in Co-Doped Barium Titanate Nanocrystals. *Nanotechnology* **2012**, *23*, No. 025702.
(70) Shah, J.; Kotnala, R. K. Induced Magnetism and Magnetoelectric Coupling in Ferroelectric $BaTiO_3$ by Cr-doping Synthesized by a Facile Chemical Route. *J. Mater. Chem. A* **2013**, *1*, 8601−8608.
(71) Cao, X.; Hong, T.; Yang, R.; Tian, J.-H.; Xia, C.; Dong, J.-C.; Li, J.-F. Insights into the Catalytic Activity of Barium Carbonate for Oxygen Reduction Reaction. *J. Phys. Chem. C* **2016**, *120*, 22895−22902.
(72) Ohgi, Y.; Ishihara, A.; Matsuzawa, K.; Mitsushima, S.; Ota, K.-i.; Matsumoto, M.; Imai, H. Oxygen reduction reaction on tantalum oxide-based catalysts prepared from TaC and TaN. *Electrochim. Acta* **2012**, *68*, 192−197.
(73) Hong, T.; Brinkman, K. S.; Xia, C. Barium Carbonate Nanoparticles as Synergistic Catalysts for the Oxygen Reduction Reaction on La0.6Sr0.4Co0.2Fe0.8O3−δ Solid-Oxide Fuel Cell Cathodes. *ChemElectroChem* **2016**, *3*, 805−813.
(74) Zhang, Z.; Sun, J.; Wang, F.; Dai, L. Efficient Oxygen Reduction Reaction (ORR) Catalysts Based on Single Iron Atoms Dispersed on a Hierarchically Structured Porous Carbon Framework. *Angew. Chem., Int. Ed.* **2018**, *57*, 9038−9043.
(75) Parvez, K.; Yang, S.; Hernandez, Y.; Winter, A.; Turchanin, A.; Feng, X.; Müllen, K. Nitrogen-Doped Graphene and Its Iron-Based Composite As Efficient Electrocatalysts for Oxygen Reduction Reaction. *ACS Nano* **2012**, *6*, 9541−9550.

https://dx.doi.org/10.1021/acsaem.0c02548
ACS Appl. Energy Mater. 2021, 4, 1313−1322